

Drag Reduction in Turbulent Flows over Superhydrophobic Surfaces

Robert J. Daniello, Nicholas E. Waterhouse and Jonathan P. Rothstein

*Department of Mechanical and Industrial Engineering, University of Massachusetts, Amherst
160 Governors Drive, Amherst, MA 01003*

Abstract

In this paper, we demonstrate that periodic, micropatterned superhydrophobic surfaces, previously noted for their ability to provide laminar flow drag reduction, are capable of reducing drag in the turbulent flow regime. Superhydrophobic surfaces contain micro or nanoscale hydrophobic features which can support a shear-free air-water interface between peaks in the surface topology. Particle image velocimetry and pressure drop measurements were used to observe significant slip velocities, shear stress, and pressure drop reductions corresponding to drag reductions approaching 50%. At a given Reynolds number, drag reduction is found to increase with increasing feature size and spacing, as in laminar flows. No observable drag reduction was noted in the laminar regime, consistent with previous experimental results for the channel geometry considered. The onset of drag reduction occurs at a critical Reynolds number where the viscous sublayer thickness approaches the scale of the superhydrophobic microfeatures and performance is seen to increase with further reduction of viscous sublayer height. These results indicate superhydrophobic surfaces may provide a significant drag reducing mechanism for marine vessels.

I. Introduction

The development of technologies which produce significant drag reduction in turbulent flows can have a profound effect on a variety of existing technologies. The benefits of drag reduction range from a reduction in the pressure drop in pipe flows to an increase in fuel efficiency and speed of marine vessels. Drag reduction in turbulent flows can be achieved through a number of different mechanisms including the addition of polymers to the fluid ¹, the addition of bubbles ² or air layers ^{3,4}, compliant walls ⁵, and riblets ⁶. We will demonstrate that superhydrophobic surfaces can be used as a new passive technique for reducing drag over a wide range of Reynolds numbers from laminar ^{7,8} to turbulent flows.

Superhydrophobic surfaces were originally inspired by the unique water repellent properties of the lotus leaf ⁹. They are rough, with micro or nanometer-sized surface features. In the Cassie state, illustrated in Figure 1, the chemical hydrophobicity of the material prevents the water from moving into the space between the peaks of the rough surface, resulting in the air-water interface which is essentially shear free. The resulting surface possesses a composite interface where momentum transfer with the wall occurs only at liquid-solid and not the liquid-vapor interfaces. Recent synthetic superhydrophobic surfaces have been developed which are perfectly hydrophobic, obtaining contact angles that can approach $\theta = 180^\circ$ with no measurable contact hysteresis ^{9,10}. It should be noted that the extreme contact angles available with superhydrophobic surfaces result from their superhydrophobic topography rather than chemical hydrophobicity; contact angles on smooth surfaces of the same chemistry are much lower.

Philip ^{11,12} and Lauga and Stone ¹³ provide analytical solutions for laminar Poiseuille flows over alternating slip and no slip boundary conditions, such as those existing above a submerged superhydrophobic surface. These results provide an analytical solution predicting and quantifying drag reduction resulting from slip/no-slip walls, in laminar flows. Ou and Rothstein ^{7,14} demonstrated that superhydrophobic surfaces produce drag reduction and an apparent slip, corresponding to slip lengths of $b = 25\mu\text{m}$, at the wall in laminar flows as a direct result of the shear-free air-water interface between surface microfeatures. Here the slip length is defined using Navier's slip model where the slip velocity, u_0 , is proportional to the shear rate experienced by the fluid at the wall

$$u_0 = b \frac{\partial u}{\partial y} \quad (1)$$

These results have been extended to a variety of superhydrophobic surface designs and flow geometries ^{8,15}. A thorough overview of the no slip boundary condition is given by Lauga *et al.* ¹⁶. Ybert *et al.* ¹⁷ examined scaling relationships for slip over superhydrophobic surfaces. For a superhydrophobic surface in the Cassie state, they showed slip length to increase sharply with decreasing solid fraction and

increasing effective contact angle¹⁷. However, Voronov *et al.*^{18, 19} demonstrated that for hydrophobic surfaces, there is not necessarily a positive correlation between increased contact angle and slip length.

Fundamentally, the effective reduction of solid-liquid boundary as a superhydrophobic drag reduction mechanism should be independent of whether the flow is laminar or turbulent. In turbulent flows, a thin viscous-dominated sublayer exists very near to the wall. It extends to a height, measured in terms of wall units, viscous lengths, of $y^+ = y/\nu\sqrt{\tau_w/\rho} = 5$ ²⁰. Where y is the height above the wall, ν is the kinematic viscosity, τ_w is the wall shear stress and ρ is the fluid density. In the viscous sublayer, the mean velocity increases linearly with position, $u^+ = y^+$. Changes in momentum transfer to the viscous sublayer can have a dramatic influence on the entire turbulent flow and can result in drag reduction. This effect is demonstrated in the direct numerical simulation (DNS) studies of Min and Kim²¹ who imposed a fixed, arbitrary, but not unreasonable, longitudinal slip length boundary condition in a turbulent channel flow. Similar work was performed by Fukagata *et al.*²² who related drag reduction and slip length. More recently, Martell *et al.*²³ used DNS to study the turbulent flows over periodic slip/no-slip boundary conditions to simulate microposts and microridges geometries that approximate the superhydrophobic surfaces presented here. Their simulations predict a drag reduction that increases with both the microfeature spacing and the surface coverage of the shear-free air-water interface as well as with the Reynolds number²⁴. In addition to the presence of the shear free interface, drag reduction mechanisms such as surface compliance and turbulent structure attenuation may also exist for micropatterned superhydrophobic surfaces.

Few experimental studies have considered superhydrophobic drag reduction into the turbulent regime²⁵⁻²⁸. In a recent experimental study, Gogte *et al.*²⁵ observed drag reduction in turbulent flow over a hydrofoil coated with a randomly structured superhydrophobic surface produced from hydrophobically-modified sandpaper. Drag reductions of up to 18%, based on combined skin friction and form drag, were reported for the hydrofoil. Overall drag reduction on the hydrofoil decreased with increasing Reynolds number. However, one should note that the total drag was reported and the individual contribution of friction and form drag were not deconvoluted. The form drag of the body should increase significantly with Reynolds number and could obscure the performance trend of the superhydrophobic surface which affects only skin friction drag. It is not necessarily inconsistent for skin friction drag reduction to be stable or increasing with Reynolds number as predicted by the DNS simulations of Martell²⁴. Balasubramanian *et al.*²⁸ achieved similar results for flow over an ellipsoidal model with a disordered superhydrophobic surface similar to that employed by Gogte *et al.*²⁵, but having smaller microfeatures. Henoch *et al.*²⁹ demonstrated preliminary success in a conference proceeding noting drag reduction over 1.25 μ m spaced “nanogras” posts in the turbulent regime.

Similar in physical mechanism to superhydrophobic drag reduction, air layer drag reduction, results from continuous air injection sufficient to produce an uninterrupted vapor layer existing between the solid surface and the water. Such air layers are an active technique for producing drag reduction; they do not require chemical hydrophobicity of the surface and exist only as long as the required air injection rate is maintained. Elbing *et al.*³ demonstrated air layers are capable of producing nearly complete elimination of skin friction drag. The authors demonstrated the existence of three distinct regions; bubble drag reduction at low air injection rates where performance is linear with air injection rate and drag reductions up to 20% can be achieved, a transitional region at moderate injection rates, and a full air layer at large air injection rates. Once the full air layer is achieved, Elbing reported little performance increase with additional airflow. It should be noted that drag reduction falls off with distance from the injection point until a complete air layer is achieved. Reed³⁰ utilized millimeter sized ridges to capture and stabilize injected air and form a continuous air layer between the ridges. The author noted hydrophobic walls, with ridge features much too large (mm) to produce a superhydrophobic effect, exhibited an enhanced ability to form and maintain stable air layers. Additionally, Fukuda *et al.*⁴ demonstrated an increase in drag reduction obtained when a discontinuous layer of injected bubbles are attracted by walls treated with hydrophobic paint.

Geometrically, riblets appear similar to the superhydrophobic surfaces under present consideration; however, their scale and function are completely different. Riblets are ridges aligned in the flow direction which reduce drag in turbulent flows by disrupting the transverse motion of the fluid at the surface, thereby moving near-wall turbulent structures farther from the wall⁶. Unlike superhydrophobic surfaces, the grooves between riblet features are wetted by the fluid, and function equally well for both liquids and gasses. Unfortunately, riblet geometries only perform well within a limited range of Reynolds numbers and can have derogatory effects outside of their designed range. To function, riblets must maintain a spacing, $w^+ = w/\nu\sqrt{\tau_w/\rho}$, between $10 < w^+ < 30$ wall units³¹. As will be demonstrated in the following sections, the superhydrophobic microfeatures used in the present experiments are at least an order of magnitude too small to produce a riblet effect. It will be shown that the observed drag reduction is due to the presence of a shear free air-water interface supported between microfeatures.

II. Experimental Procedure

The present work presents particle image velocimetry (PIV) and pressure drop measurements of a turbulent channel flow over several superhydrophobic walls. The superhydrophobic surfaces were engineered with regular arrays of microridges aligned in the flow direction in order to systematically investigate the effect of topological changes on the velocity profiles, slip length and drag reduction in turbulent channel flows. Superhydrophobic PDMS test surfaces were cast from silicon wafer molds

produced by a lithographic process. A $25\mu\text{m}$ layer of SU 8 photoresist (Microchem) was spun onto bare or oxide coated silicon wafers. The substrate was then exposed through a negative mask of the desired pattern and developed to produce a mold. A micrograph of a typical wafer mold, in this case for $60\mu\text{m}$ microridges spaced $60\mu\text{m}$ apart, is shown in Figure 1b. Once completed, the wafers were used to cast patches of micropatterned PDMS approximately 150mm long which were then seamlessly joined to produce a 1m long superhydrophobic surface. All measurements are conducted on the downstream section of the patch, minimally thirty channel half heights, δ , downstream of the nearest patch joint. Smooth test surfaces were prepared by curing PDMS on a smooth flat cast PMMA plate. The PDMS was treated with a highly fluorinated silane (Gelest, Tullytown, PA) to make it more hydrophobic, resulting in an advancing contact angle of approximately $\theta = 125^\circ$. Untreated PDMS having an advancing contact angle of approximately $\theta = 110^\circ$ on a smooth surface was also used with identical results. No measurable slip lengths were observed for flows over smooth PDMS surfaces. It should be noted that for materials not demonstrating slip over smooth surfaces, contact angle is important to superhydrophobicity only inasmuch as it increases the maximum pressure sustainable by the three phase interface⁷. Contact angle does not affect the shear free area or the interface deflection for a fixed sustainable pressure, and thus should not affect the turbulent drag reduction obtained. A section of microridge superhydrophobic surface is seen in Figure 2 with two droplets of water, sitting on top of the microfeatures, demonstrating the Cassie state, and ethanol, which wets the surface, demonstrating the Wenzel state.

PIV is conducted in a rectangular channel flow geometry shown in Figure 3a., fabricated from optically clear polymethyl methacrylate (PMMA) with a single interchangeable polydimethylsiloxane (PDMS) test surface at the bottom wall. The channel was $W = 38.1\text{mm}$ wide and full channel height was $2\delta = 7.9\text{mm}$. Reverse osmosis purified water was used as the working fluid. Water purity does not seem to affect drag reduction results the same water was used for several weeks with no change in performance. For PIV, the water was seeded with 0.005wt% of $1\mu\text{m}$ diameter hollow silvered glass spheres (Sphericul, Potters Industries, Carlstadt, NJ). Flow was provided under gravity from a head tank and collected for reuse. A centrifugal pump returns fluid to maintain head level, provisions exist to run the apparatus directly from the pump although, to reduce vibrations, the pump is turned off during measurements. Static pressures within the flowcell were held below 5kPa to ensure the Cassie state was maintained. Ridges were designed to prevent air from escaping at the ends and to allow operation near or possibly above the limit predicted by Young's law for captive air at atmospheric pressure. The flow rate was measured by one of two turbine flow meters (low flow rates FTB-603, Omega; high flow rates FTB-902, Omega) placed in series with the test section. It was adjusted by a throttling valve located far upstream. Reynolds number was calculated from flow rate and verified by numerical integration of velocity profiles when PIV profiles of the entire channel height were accessible. PIV was conducted in the x - y plane at mid channel

approximately 200-225 half heights from the inlet, far enough downstream to ensure a fully developed turbulent flow over the superhydrophobic surfaces. Illumination is provided by a 500 μm wide light sheet. Images were recorded with a high-speed video camera (Phantom 4.2) at frame rates up to 8500 frame per second and correlated with a commercial code (DaVis, LaVision GmbH). Under the maximum magnification of our experiments, the velocities could be accurately resolved within 50 μm from the wall. At reduced magnifications, PIV images cover the entire channel to simultaneously observe smooth top and superhydrophobic bottom walls. Images were recorded under ambient lighting to establish wall location; for full channel measurements the true wall location is known to within 10 μm accuracy. Up to 10,000 frames of steady state flow were captured, correlated and averaged to generate each velocity profile. Scale was established by imaging targets and verified with the known height of the channel.

Presently, we consider two superhydrophobic microridge geometries and the smooth PMMA top wall, which have been tested over a range of mean Reynolds numbers $2000 < Re = 2\delta U / \nu < 9500$. Here U is the mean fluid velocity measured from the flow. Transitional effects are considered to persist up to $Re = 3000$ for this flow²⁰. Two geometries with 50% shear-free air-water interface coverage were considered. The first contains microridges $d = 30\mu\text{m}$ wide and spaced $w = 30\mu\text{m}$ apart (30-30) and the second contained microridges $d = 60\mu\text{m}$ wide and spaced $w = 60\mu\text{m}$ apart (60-60). As noted, feature sizes considered range from $w^+ < 2$ wall units for the 30-30 ridges and remain less than $w^+ < 3.5$ wall units for the 60-60 ridges. These ridge spacings are an order of magnitude too small to produce a riblet effect over the present range of Reynolds numbers.

Additional quantification of superhydrophobic drag reduction was obtained through direct pressure drop measurements in the channel. Here, the test section was replaced with a channel having superhydrophobic surfaces on both top and bottom walls, Figure 4. The channel height was set by the precisely machined aluminum side spacer seen in the figure, and the flowcell assembly was conducted with a calibrated wrench to maintain precise uniformity of the channel between tests, fixing the channel aspect ratio. The channel was $W = 38.1\text{mm}$ wide and $2\delta = 5.5\text{mm}$ high. Additionally, multiple data collection sessions were performed for each surface, with reassembly of the apparatus between each session. Measurements were conducted from single taps, as illustrated, over a 70mm span more than 130δ from the channel inlet. Pressure was read directly from a pair of water column manometers reading static pressures at the front and back of the test section. Water column heights were photographically recorded, the differences in column height being used to calculate the pressure drop across the test section. The manometer resolution was $\pm 1\text{Pa}$, which resulted in pressure drop measurement uncertainty that ranged from 5% for the slowest flows to 0.5% for the highest Reynolds numbers tested. Flow rate was measured with a turbine flow meter as in the PIV experiments. Flow control and Reynolds number capabilities are identical to those used for PIV. To ensure steady state, data points were taken no more

than once per minute and the flow rate was adjusted only incrementally between measurements. Data was collected on increasing and decreasing flow rate sweeps to ensure that no hysteresis was observed.

III. Results and Discussion

A typical set of velocity profiles, resulting from PIV near the superhydrophobic wall for the 60-60 ridge surface is shown in Figure 5a for a range of Reynolds number between $2700 < Re < 8200$. The effect of the superhydrophobic wall is not observed for the low Reynolds number experiments. At the low Reynolds numbers, the turbulent velocity profiles just past transition are, to the limit of our measurements, equivalent to smooth profiles at identical Reynolds numbers. This is not unexpected for the data points in the laminar or transitional regime^{7, 14}. In laminar flows, superhydrophobic surfaces of similar size and geometry demonstrated slip lengths which were independent of flow rate and approximately $b = 25\mu\text{m}$ ¹⁴. For pressure driven flow between two infinite parallel plates separated by a distance 2δ the volume flow rate per unit depth is given by

$$q = \frac{2\delta^3}{\mu} \left(-\frac{dp}{dx} \right) \left[\frac{1}{3} + \frac{b}{b + 2\delta} \right]. \quad (2)$$

For a given pressure gradient, dp/dx , and fluid viscosity, μ , the volume flow rate can be significantly enhanced only if the slip length is comparable to the channel height. Previous laminar regime studies over similar superhydrophobic microfeatures measured slip lengths of $b = 25\mu\text{m}$ independent of Reynolds number⁷. In our channel geometry, such laminar flow slip lengths would produce a drag reduction of around 1%. Additionally, for small slip lengths, the expected slip velocity can be approximated by $u_{\text{slip}} = 4U b / \delta$ which should also be on the order of only a couple of percent of the average free stream velocity, U , and below the resolution of our PIV measurements. As the Reynolds number is increased and the flow becomes fully turbulent, however, a substantial slip velocity, and slip lengths greater than $b = 25\mu\text{m}$, are observed along the superhydrophobic wall. The presence of an air water interface is visually apparent on the superhydrophobic surface giving it a silvery appearance. This result, due to the differing indices of refraction and slight curvature of the interface, was observed throughout the range of testing giving us confidence that the interface was maintained for all of the experiments reported in this paper.

As the inset of Figure 5a clearly shows, the magnitude of the slip velocity was found to increase with increasing Reynolds number. Similar, although less pronounced, trends were observed for the 30-30 ridge case as seen in Figure 5b. Significant deviation from no-slip behavior is noted past a Reynolds number of approximately $Re = 4000$ for both the 30-30 and 60-60 ridged cases. Above these Reynolds numbers, a nearly linear increase in the slip velocity with increasing Reynolds number was observed for

each of the superhydrophobic surfaces used. A maximum slip velocity of nearly 40% the mean channel velocity, $u_{slip}/U = 0.4$ was observed for the 60-60 ridged case at the highest Reynolds numbers tested.

In order to determine both the shear stress and slip velocity at the smooth and superhydrophobic walls, the PIV velocity fields were fit to a modified Spalding equation for turbulent velocity profile above a flat plate³²,

$$y^+ = (u^+ - u_{slip}^+) + e^{-2.05} \left[e^{-0.41(u^+ - u_{slip}^+)} - 1 - 0.41(u^+ - u_{slip}^+) - \frac{1}{2}(0.41(u^+ - u_{slip}^+))^2 - \frac{1}{6}(0.41(u^+ - u_{slip}^+))^3 \right]. \quad (3)$$

The Spalding equation is an empirical fit to experimental turbulent velocity profile data that covers the entire wall region through the log layer³³. This allows the fit to be applied farther into the channel, to determine the wall shear stress more accurately using a greater number of data points than would be available within the viscous sublayer. Wall shear stress enters the equation in the definition of the velocity, u^+ , and position y^+ , in wall units. To account for slip, each instance of the velocity in wall units, $u^+ = u\sqrt{\rho/\tau_w}$, in the Spalding equation was replaced by the difference $u^+ - u_{slip}^+$. The fit was performed by a numerical routine given an initial value for slip velocity extrapolated from a coarse linear fit of near wall data points. An initial wall shear stress was determined by minimizing the error in the fit. Subsequent iterations were performed on wall slip velocity and wall shear stress to minimize the standard error of the fit over the interval $0 < y^+ < 50$. The resulting fits were accurate to better than 4% at a 95% confidence interval. The results were not appreciably different if the fit is taken to $y^+ = 100$. The size of the PIV correlation window was chosen to be 0.2mm. For the frame rates used, the resulting particle displacements within the correlation window were typically much less than 25% of the window in the viscous sublayer and less than 33% of the window everywhere for Reynolds numbers less than $Re < 4500$. Large particle displacements were observed far from the wall at the highest Reynolds numbers, however, no noticeable effects were observed on the resulting profiles.

As seen in Figure 5, the resulting fits of Equation 3 to the velocity profiles are excellent with and without slip, which instills confidence in the values of shear stress calculated from the velocity gradient extrapolated to the wall, $\tau_w = \mu (\partial u / \partial y)|_{y=0}$. The maximum slip velocity and observed wall shear stress reductions correspond to slip lengths of $b > 70\mu\text{m}$ for the 30-30 microridges and $b > 120\mu\text{m}$ for the 60-60 microridges. Larger slip velocities and slip lengths were measured for turbulent flow past superhydrophobic surfaces with larger microfeature spacings even as the percentage of shear-free interface was kept constant at $w/(w+d) = 0.5$, as has been observed in the laminar flow measurements over superhydrophobic surfaces¹⁴. This observation is consistent previous laminar flow studies^{7, 14} and with the predictions of DNS in turbulent flows²⁴. Additionally, Ybert *et al.*¹⁷ showed through a scaling

argument that in laminar flows one expects the slip length to scale linearly with the microfeature spacing, $b \propto (w + d)$.

In Figure 6, direct measurements of the pressure drop per unit length of channel, dp/l , are shown for a smooth PDMS surface and the superhydrophobic surface containing 60 μ m ridges spaced 60 μ m apart in an identical channel. The result predicted by the Colebrook equation³⁴ for a perfectly smooth channel of the same dimension is plotted for reference. The pressure drop per unit length is directly related to the channel geometry and the wall shear stress, $dp/l = \tau_w (1 + 2\delta/W)/\delta$, so it provides a second method for measuring drag reduction. Significant drag reduction is initially noted by a leveling off of the in the pressure drop during the transition from laminar to turbulent flow between Reynolds numbers of $2000 < Re < 3000$. These data indicate a delay in the transition to fully-developed turbulent flow. Additionally, for Reynolds numbers greater than $Re > 3000$ the pressure drop over the superhydrophobic surface grows at roughly have the rate of pressure drop over the smooth surface. The Colebrook line, accurately fits the turbulent flow data from the smooth surface, and the predicted laminar flow result passes through the microridge data in the laminar region below $Re < 2200$. This result is consistent with those predicted by Equation 2 and observed by PIV. As noted before there is no measurable drag reduction or slip velocity for the present channel geometry in the laminar regime.

Further insight comes from the full channel PIV where smooth and superhydrophobic surfaces may be simultaneously observed at the same mean channel Reynolds numbers. Wall shear stress, calculated from the modified Spalding fits, is shown in Figure 7 for the smooth and superhydrophobic surfaces. Again the Colebrook line for a channel of the same dimensions is shown for comparison. Shear stress reduction on the superhydrophobic wall follows the same trends observed from pressure measurements in Figure 6. Little significant drag reduction is observed $Re < 3000$ with a marked reduction in rate of shear stress increase for $Re > 5000$. The smooth wall behaves as expected for an entirely smooth channel, as indicated by the good agreement with the Colebrook line.

In Figure 8, the wall shear stresses, τ_w , calculated from the Spalding fit to the velocity profiles and from pressure measurements of smooth, 30-30 and 60-60 channels are non-dimensionalized to form a coefficient of friction, $C_f = 2\tau_{wall} / \rho U^2$, and plotted as a function of Reynolds number. For comparison, the Colebrook prediction of friction coefficient for the present perfectly smooth channel is superimposed over the data in Figure 8. Friction coefficient was selected to account for small variations in channel height existing between the pressure drop and PIV experiments. As previously indicated, the friction coefficients of the smooth wall, calculated from PIV, and that of the smooth channel, determined from pressure drop, are in good agreement with each other as well as with the Colebrook prediction. At low Reynolds numbers, in the absence of any quantifiable slip at the superhydrophobic wall, the coefficient of

friction for all cases tracks with that of the smooth-walled channel. At larger Reynolds numbers, where slip velocities are observed, the coefficients of friction of the superhydrophobic surfaces were found to lie well below those of the smooth channels. The drag reduction was found to increase with increasing Reynolds number, becoming more significant for $Re > 5000$ as observed in the pressure measurements. The PIV measurements of the channel with a 30-30 superhydrophobic microridge surface on one wall and a smooth no-slip surface on the opposing wall show a somewhat smaller drag reduction than that which is noted by pressure drop along with two superhydrophobic walls. This result is likely due to differences in the flowcell geometry, specifically, the presence of the smooth wall in the PIV measurements, which was necessary to have transparency for flow visualization. The smooth wall has a higher wall shear stress than the superhydrophobic surface resulting in an asymmetric velocity profile and an increase in the turbulence intensity near the smooth wall. These observations were also made by Martell *et al.*^{24, 23} for a DNS of channel flow with a single superhydrophobic wall. Observed drag reductions and slip velocities are in good agreement with predictions for a DNS at $Re_\tau = 180$, corresponding to an experimental $Re = 5300$ in the PIV data. DNS slightly over predicts slip velocity, and slightly under predicts drag reduction at 11% and reports enhanced performance with increasing microfeature size, as observed in the experiments. It should also be noted that DNS of Martell *et al.*^{24, 23} does not include interface deflection or compliance effects. Drag reduction calculated from PIV data are in excellent agreement with the slip length boundary condition DNS of Min and Kim²¹ and predictions of Fukagata *et al.*²² for streamwise slip. Both groups reported approximately 21% drag reduction^{21, 22} at the same dimensionless slip length and friction Reynolds number observed in the present experiments at $Re = 5300$. Given the challenges of directly matching DNS and experiments, these results are quite encouraging.

The turbulent drag reduction, $D_R = (\tau_{no-slip} - \tau_{SH}) / \tau_{no-slip}$, was computed as the percent difference in shear stress at the superhydrophobic and no-slip wall and is presented in Figure 9 as a function of Reynolds number. Drag reduction is presented rather than slip length because the slip length is difficult to quantify from the pressure drop measurements in turbulent flows. The slip length calculated from PIV data is insignificant in the laminar region and obtains a maximum value greater than $b = 70\mu\text{m}$ for 30-30 and greater than $b = 120\mu\text{m}$ for 60-60 ridges. In the present experiments, a maximum drag reduction of approximately 50% was observed for both microridge geometries once a suitably high Reynolds number was achieved. Drag reduction is initiated at a critical Reynolds number in the turbulent regime. For the microridges under present consideration, the critical Reynolds number was determined to be $Re_{crit} \approx 2500$. This Reynolds number is at or just past the transition to turbulent flow. This observation, along with the noted lack of drag reduction in the laminar regime, suggest that the underlying physical cause of the observed turbulent drag reduction must relate to the unique structure of wall-bounded turbulent flow.

The physical origins of the critical Reynolds number for the onset of drag reduction can be understood by analyzing the relevant lengthscales in the flow. If the drag reduction and the slip length were dependent on the microridge geometry and channel dimensions alone, as is the case in laminar flows, then we would expect to find the drag reduction and slip length to be independent of Reynolds number. In turbulent flows, however, there is a third lengthscale of importance, the thickness of the viscous sublayer which extends out to $y^+ = 5$. Although the viscous sublayer thickness remains fixed in wall units, in dimensional form the thickness of the viscous sublayer decreases with increasing Reynolds number as $y_{vsl} = 5\nu\sqrt{\rho/\tau_w}$. Close to the wall, where viscous stresses dominate, the analytical solutions of Philip^{11, 12} show that the influence of the shear-free air-water interface extends to a distance roughly equal to the microridge spacing, w , into the flow. Thus for the superhydrophobic surface to impact the turbulent flow, the microridge spacing must approach the thickness of the viscous sublayer, $w \approx y_{vsl}$, or in other words $w^+ = y^+ \approx 5$. As seen in Figure 10, the microfeature spacing in wall units is at least $w^+ > 0.75$ for all the 30-30 surfaces tested and $w^+ > 2.4$ for the 60-60 surfaces. The w^+ values are calculated from shear stress measured at the superhydrophobic surface. This means that the microfeature spacing is minimally 15% to 50% of viscous sublayer thickness almost immediately after the turbulent transition. Hence for 30-30 and 60-60 ridges, drag reduction is noticed almost as soon as a turbulent flow develops. In laminar flows, significant drag reduction is noted at feature to height ratios comparable to those seen with the present feature size and viscous sublayer thickness³⁵. A similar scaling has been observed for turbulent flow over wetted, rough surfaces, where the effects of roughness are not observed until the size of the roughness exceeds the thickness of the viscous sublayer³⁶. As the Reynolds number increases and the thickness of the viscous sublayer is further reduced, the presence of the superhydrophobic surface will more strongly influence the velocity profile within the viscous sublayer and reduce the momentum transferred from the fluid to the wall and the vorticity of the fluid at the edge of the viscous sublayer. Turbulence intensity is thereby reduced, increasing the drag reduction. One therefore expects that saturation of the turbulent drag reduction is likely in the limit of very large Reynolds numbers where the microridges are much larger than the viscous sublayer. In this limit, the drag reduction should approach a limit of $D_R = w/(d + w)$ as momentum is only transferred from the solid fraction of the superhydrophobic surface and the viscous sublayer is thin enough that the no-slip and shear-free portions of the surface can be considered independently. For the present shear free area ratios, this limit would be 50%. This is consistent with both the asymptotic value of our PIV and pressure drop measurements. Drag reduction results shown in Figure 9 appear consistent with this hypothesis, the 60-60 ridges already appearing to plateau. As the critical Reynolds number will decrease with increasing feature spacing, coarser superhydrophobic surfaces will begin to perform better at lower Reynolds numbers. It is therefore

expected that equivalent drag reduction performance will be accessible to much finer microfeature spacings at higher Reynolds numbers. With fine superhydrophobic surfaces, little drag reduction may be evident until the viscous sublayer shrinks significantly, well past transition. This result appears promising for possible commercial applications of this technology. This is because small feature spacing results in a more robust superhydrophobic surface capable of maintaining a coherent air-water interface at larger static pressures, while at the same time ships that might benefit from such surfaces operate at Reynolds numbers significantly greater than those interrogated in the present experiments.

IV. Conclusions

Significant drag reduction has been measured by PIV and direct pressure measurements in turbulent flows over superhydrophobic microridge surfaces. No significant drag reduction or slip velocities were noted in the laminar regime, consistent with theoretical predictions of laminar flow superhydrophobic drag reduction and previous experimental studies. This and the slip velocities observed at the wall demonstrate that the drag reduction is due to the presence of a shear-free interface. Slip velocities and drag reductions were found to increase with Reynolds number, the latter appearing to plateau at the highest Reynolds numbers tested. This drag reduction is found to increase more quickly with increasing feature spacing for equal shear free area ratio. Our experiments suggest that viscous sublayer thickness is the correct height scaling for these surfaces and there exists a critical Reynolds number reached as the viscous sublayer thickness approaches microfeature size, when the onset of drag reduction will occur. Additional experiments and numerical simulations are currently underway to investigate this hypothesis.

V. Acknowledgments

The authors wish to acknowledge the Office of Naval Research for the support provided for this research under grant N00014-06-1-0497. The authors would also like to thank M. Martell and B. Perot for helpful discussions and suggestions.

VI. References

- ¹ P. S. Virk, "Drag reduction fundamentals," *AICHE J.* **21**, 625 (1975).
- ² W. C. Sanders, E. S. Winkel, D. R. Dowling, M. Perlin, and S. L. Ceccio, "Bubble friction drag reduction in a high-reynolds-number flat-plate turbulent boundary layer," *J. Fluid Mech.* **552**, 353 (2006).
- ³ B. Elbing, R., E. Winkel, S., K. Lay, S., S. Ceccio, L., D. Dowling, R., and M. Perlin, "Bubble-induced skin-friction drag reduction and the abrupt transition to air-layer drag reduction," *Journal of Fluid Mechanics* **612**, 201 (2008).
- ⁴ K. Fukuda, J. Tokunaga, T. Nobunaga, T. Nakatani, T. Iwasaki, and Y. Kunitake, "Frictional drag reduction with air lubricant over a super-water-repellent surface," *Journal of Marine Science and Technology* **5**, 123 (2000).
- ⁵ S. Hahn, J. Je, and H. Choi, "Direct numerical simulation of turbulent channel flow with permeable walls," *J. Fluid Mech.* **450**, 259 (2002).
- ⁶ D. W. Bechert, M. Bruse, W. Hage, J. G. T. van der Hoeven, and G. Hoppe, "Experiments in drag-reducing surfaces and their optimization with an adjustable geometry," *J. Fluid Mech.* **338**, 59 (1997).
- ⁷ J. Ou, J. B. Perot, and J. P. Rothstein, "Laminar drag reduction in microchannels using ultrahydrophobic surfaces," *Phys. Fluids* **16**, 4635 (2004).
- ⁸ P. Joseph, C. Cottin-Bizonne, J.-M. Benoit, C. Ybert, C. Journet, P. Tabeling, and L. Bocquet, "Slippage of water past superhydrophobic carbon nanotube forests in microchannels," *Phys. Rev. Lett.* **97**, 156104 (2006).
- ⁹ D. Quere and M. Reyssat, "Non-adhesive lotus and other hydrophobic materials," *Phil. Trans. Roy. Soc. A* **366**, 1539–1556 (2008).
- ¹⁰ L. Gao and T. McCarthy, J., "A Commercially Available Perfectly Hydrophobic Material *Langmuir* **23**, pp. 9125 (2007).
- ¹¹ J. R. Philip, "Integral properties of flows satisfying mixed no-slip and no-shear conditions," *Z. Angew. Math. Phys.* **23**, 960 (1972).
- ¹² J. R. Philip, "Flows satisfying mixed no-slip and no-shear conditions," *Z. Angew. Math. Phys.* **23**, 353 (1972).
- ¹³ E. Lauga and H. A. Stone, "Effective slip in pressure-driven Stokes flow," *Journal of Fluid Mechanics* **489**, 55 (2003).
- ¹⁴ J. Ou and J. P. Rothstein, "Direct velocity measurements of the flow past drag-reducing ultrahydrophobic surfaces," *Phys. Fluids* **17**, 103606 (2005).
- ¹⁵ R. Truesdell, A. Mammoli, P. Vorobieff, P. van Swol, and C. J. Brinker, "Drag Reduction on a Patterned Superhydrophobic Surface," *Physical Review Letters* **97**, 044504 (2006).
- ¹⁶ E. Lauga, M. P. Brenner, and H. A. Stone, in *Handbook of Experimental Fluid Dynamics*, edited by J. Foss, C. Tropea and A. L. Yarin (Springer, New York, 2007).
- ¹⁷ C. Ybert, C. Barentin, C. Cottin-Bizonne, P. Joseph, and L. Bocquet, "Achieving large slip with superhydrophobic surfaces: Scaling laws for generic geometries," *Physics of Fluids* **v 19**, p 123601 (2007).
- ¹⁸ R. S. Voronov, D. V. Papavassiliou, and L. L. Lee, "Review of Fluid Slip over Superhydrophobic Surfaces and Its Dependence on the Contact Angle," *Ind. Eng. Chem. Res.* **47**, 2455 (2008).
- ¹⁹ R. S. Voronov, D. V. Papavassiliou, and L. L. Lee, "Boundary slip and wetting properties of interfaces: Correlation of the contact angle with the slip length," *Journal of Chemical Physics* **124**, 204701 (2006).
- ²⁰ S. B. Pope, *Turbulent Flows* (Cambridge University Press, Cambridge, UK, 2003).
- ²¹ T. Min and J. Kim, "Effects of hydrophobic surface on skin-friction drag," *Physics of Fluids* **16**, L55 (2004).

22 K. Fukagata, N. Kasagi, and P. Koumoutsakos, "A theoretical prediction of friction drag
 23 reduction in turbulent flow by superhydrophobic surfaces," *Physics of Fluids* **18**, 051703 (2006).
 24 M. Martell, B., J. Rothstein, P., and J. Perot, B., "Direct Numerical Simulation of Turbulent Flow
 25 over Ultrahydrophobic Surfaces," *J. Fluid Mech.* **620**, 31 (2009).
 26 M. Martell, B., in *Department of Mechanical and Industrial Engineering* (University of
 27 Massachusetts, Amherst, 2008), p. 127.
 28 S. Gogte, P. Vorobieff, R. Truesdell, A. Mammoli, F. van Swol, P. Shah, and C. J. Brinker,
 29 "Effective slip on textured superhydrophobic surfaces," *Physics of Fluids* **17** (2005).
 30 C. Henoch, T. N. Krupenkin, P. Kolodner, J. A. Taylor, M. S. Hodes, A. M. Lyons, C. Peguero,
 31 and K. Breuer, "Turbulent Drag Reduction Using Superhydrophobic Surfaces," *Collection of
 32 Technical Papers - 3rd AIAA Flow Control Conference* **2**, p 840 (2006).
 33 K. Watanabe, Yanuar, and H. Udagawa, "Drag reduction of Newtonian fluid in a circular pipe
 34 with highly water-repellent wall," *J. Fluid Mech.* **381**, 225 (1999).
 35 A. Balasubramanian, K., A. Miller, C., and O. Rediniotis, K., "Microstructured Hydrophobic skin
 36 for Hydrodynamic Drag Reduction," *AIAA Journal* **42**, 411 (2003).
 C. Henoch, T. N. Krupenkin, P. Kolodner, J. A. Taylor, M. S. Hodes, A. M. Lyons, C. Peguero,
 and K. Breuer, *Turbulent Drag Reduction Using Superhydrophobic Surfaces* (AIAA, Reston, VA,
 2006).
 J. Reed, C., "Using Grooved Surfaces to Improve the Efficiency of Air Injection Drag Reduction
 Methods in Hydrodynamic Flows," *Journal of Ship Research* **38**, 133 (1994).
 D. B. Goldstein and T.-C. Tuan, "Secondary flow induced by riblets," *J. Fluid Mech.* **363**, 115
 (1998).
 F. White, M., *Viscous Fluid Flow* (McGraw-Hill, Boston, 2006).
 D. Spalding, B., "A Single Formula for the "Law of the Wall"," *ASME Journal of Applied
 Mechanics Series E*, 455 (1961).
 L. Moody, F., "Friction Factors for Pipe Flow," *American Society of Mechanical Engineers --
 Transactions* **66**, 671 (1944).
 J. Ou and J. P. Rothstein, "Direct velocity measurements of the flow past drag-reducing
 ultrahydrophobic surfaces," *Physics of Fluids* **17** (2005).
 F. M. White, *Viscous Fluid Flow* (McGraw-Hill, New York, 1991).

List of Figure Captions

Figure 1. Schematic diagram of air trapped between hydrophobic microfeatures of a superhydrophobic surface. The air-water interface produces shear free regions resulting in a reduction in wetted area and regions that can experience significant slip in flows. (b) Micrograph of a superhydrophobic microridge geometry containing $60\mu\text{m}$ wide ridges spaced $60\mu\text{m}$ apart. Features are approximately $25\mu\text{m}$ deep.

Figure 2. Water and ethanol droplets resting on a superhydrophobic surface. The water drops stand off the surface in the Cassie state while ethanol fully wets the surface in the Wenzel state. Microridges run front to back and the air-water interfaces they support are visible under the water drops.

Figure 3. Cross section of flow cell used for PIV with a PDMS superhydrophobic surface on the bottom and a smooth acrylic surface on top. The bottom surface was interchangeable and was replaced with a number of different superhydrophobic PDMS surfaces.

Figure 4. Cross section of flow cell used for pressure drop measurements. Superhydrophobic surfaces were fitted to both the top and the bottom surfaces of the channel.

Figure 5. a.) Velocity profiles over a microridge surface $w = 60\mu\text{m}$ $d = 60\mu\text{m}$ showing the development of significant slip velocities with increasing Reynolds number from 2700 (Δ) to 8200 (\blacksquare). (Inset) Velocity profiles near the wall demonstrating prominent slip velocities. Reynolds numbers are: 2700 (Δ), 3900 (\blacktriangle), 4840 (\diamond), 5150 (\blacklozenge), 6960 (\square), 8200 (\blacksquare). For clarity, the modified Spalding fits (—) from Equation 3 are only overlaid on the profiles corresponding to $Re=2700$ and $Re=8200$. b.) Velocity profiles over the $w = 30\mu\text{m}$ $d = 30\mu\text{m}$ microridge surface demonstrate slip velocity behavior consistent with that observed on the 60-60 surface, but reduced in magnitude. Reynolds numbers range from 4970 (\circ) to 7930 (∇). Larger feature spacing performs better for a given Reynolds number. Reynolds numbers are: 4970 (\circ), 5400 (\blacklozenge), 6800 (Δ), 7160 (\blacksquare), 7930 (∇). The modified Spalding fits (—) are overlaid on the profile corresponding to $Re=7930$.

Figure 6. Pressure drop measurements for flow through a rectangular channel with a smooth walls (Δ) and with two walls containing superhydrophobic microridges with $w=60\mu\text{m}$ and $d=60\mu\text{m}$ (\blacksquare). The Colebrook line (—) is shown for a smooth channel.

Figure 7. Wall shear stress measured from PIV as a function of Reynolds number for a channel with a single superhydrophobic surface. Results are presented for both the smooth top wall (Δ) and the superhydrophobic bottom wall containing $w=30\mu\text{m}$ wide ridges spaced $d=30\mu\text{m}$ apart (\bullet). Drag reduction is seen only on the superhydrophobic wall, the smooth wall being in good agreement with the Colebrook prediction for a smooth channel (—).

Figure 8. Coefficient of friction for various surfaces calculated from both PIV and pressure measurements. Smooth surfaces (Δ) and superhydrophobic surfaces containing $w=30\mu\text{m}$ wide microridge spaced $d=30\mu\text{m}$ apart (\bullet) are shown for PIV measurements of a channel with a single superhydrophobic wall. Pressure drop measurements from channels with two smooth walls (\star) and two superhydrophobic walls containing $w=30\mu\text{m}$ and $d=30\mu\text{m}$ microridges (\circ) and $w=60\mu\text{m}$ $d=60\mu\text{m}$ microridges (\blacksquare) are also shown. The predictions of the friction coefficient for a smooth channel is also shown (—) in both the laminar and turbulent regimes. Transition occurs around $Re = 2100$.

Figure 9. Drag reduction as a function of Reynolds number for a channel with a) a single superhydrophobic wall $w=30\mu\text{m}$ $d=30\mu\text{m}$ (●) and b) two superhydrophobic walls containing $w=30\mu\text{m}$ and $d=30\mu\text{m}$ microridges (○) and $w=60\mu\text{m}$ and $d=60\mu\text{m}$ microridges (■).

Figure 10. The microridge spacing in wall units, w^+ , as a function of Reynolds number. The data are taken from PIV measurements from a channel with a single superhydrophobic surface of $w=30\mu\text{m}$ and $d=30\mu\text{m}$ microridges (●) and from pressure measurements for flow through a channel with two superhydrophobic walls containing $w=30\mu\text{m}$ and $d=30\mu\text{m}$ microridges (○) and $w=60\mu\text{m}$ and $d=60\mu\text{m}$ microridges (■). A spacing of $w^+ = 5$ corresponds to the thickness of the viscous sublayer. Only points in the turbulent regime are shown.

Figure 1

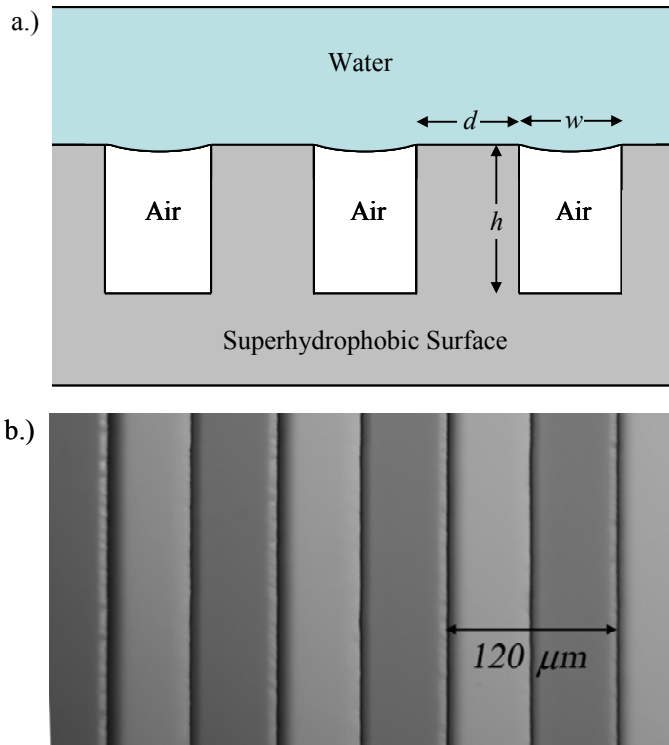


Figure 1. Schematic diagram of air trapped between hydrophobic microfeatures of a superhydrophobic surface. The air water interface produces shear free regions resulting in a reduction in wetted area and regions that can experience significant slip in flows. (b) Micrograph of a superhydrophobic microridge geometry containing $60\ \mu\text{m}$ wide ridges spaced $60\ \mu\text{m}$ apart. Features are approximately $25\ \mu\text{m}$ deep.

Figure 2.

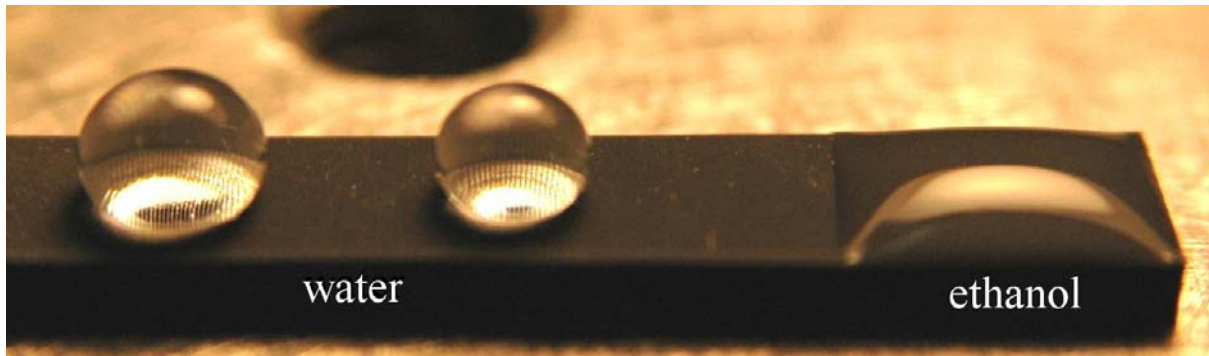


Figure 2. Water and ethanol droplets resting on a superhydrophobic surface. The water drops stand off the surface in the Cassie state while ethanol fully wets the surface in the Wenzel state. Microridges run front to back and the air-water interfaces they support are visible under the water drops.

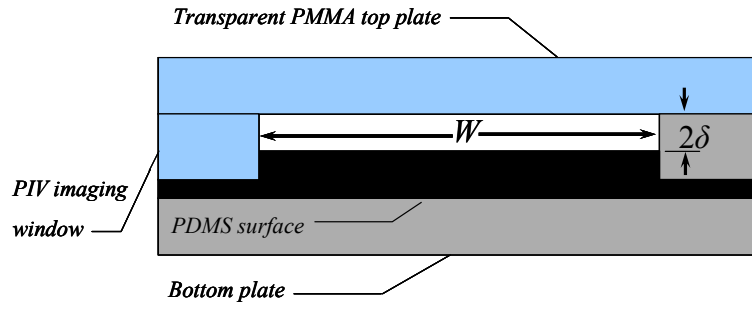


Figure 3. Cross section of flow cell used for PIV with a PDMS superhydrophobic surface on the bottom and a smooth acrylic surface on top. The bottom surface was interchangeable and was replaced with a number of different superhydrophobic PDMS surfaces.

Figure 3.

Figure 4.

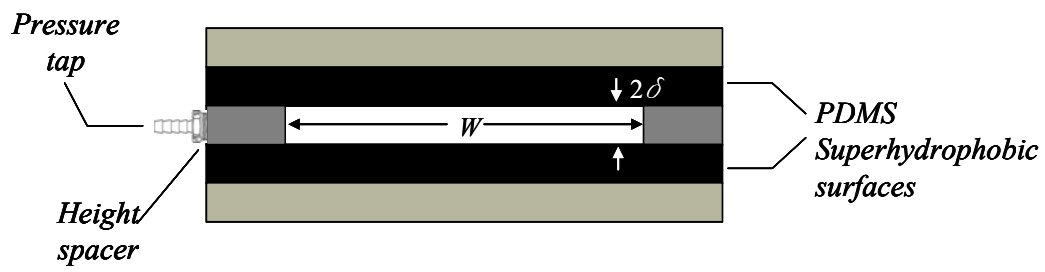


Figure 4. Cross section of flow cell used for pressure drop measurements. Superhydrophobic surfaces were fitted to both the top and the bottom surfaces of the channel.

Figure 5.

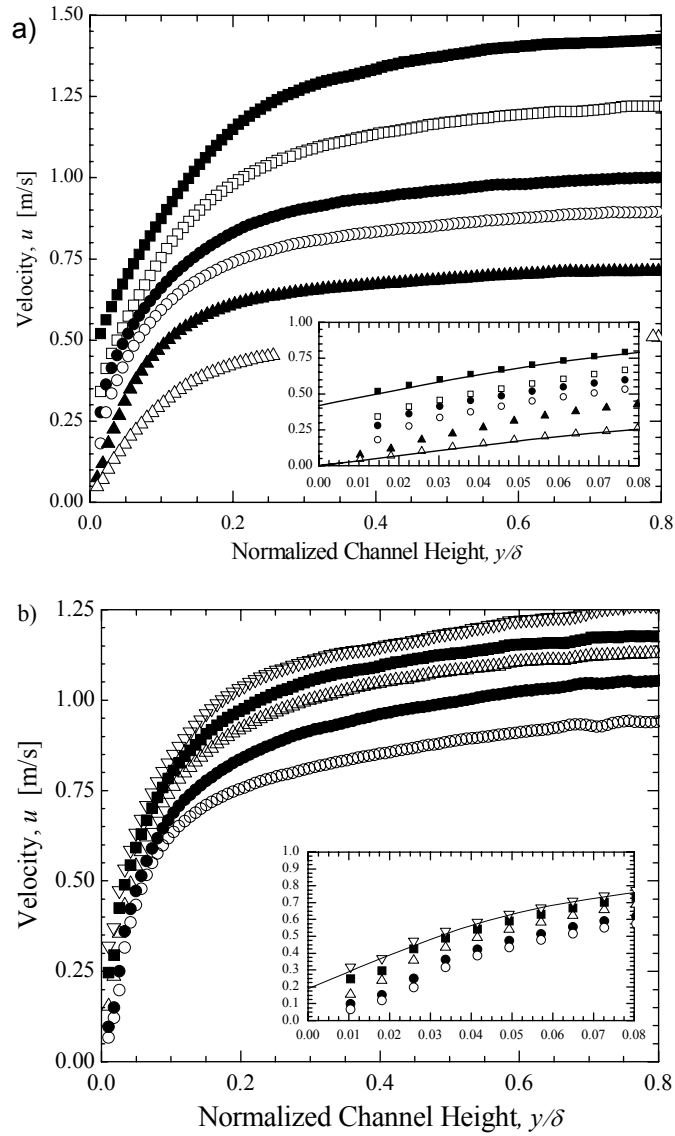


Figure 5. a.) Velocity profiles over a microridge surface $w = 60\mu\text{m}$ $d = 60\mu\text{m}$ showing the development of significant slip velocities with increasing Reynolds number from 2700 (Δ) to 8200 (\blacksquare). (Inset) Velocity profiles near the wall demonstrating prominent slip velocities. Reynolds numbers are: 2700 (Δ), 3900 (\blacktriangle), 4840 (\diamond), 5150 (\blacklozenge), 6960 (\square), 8200 (\blacksquare). For clarity, the modified Spalding fits (—) from Equation 3 are only overlaid on the profiles corresponding to $Re=2700$ and $Re=8200$. b.) Velocity profiles over the $w = 30\mu\text{m}$ $d = 30\mu\text{m}$ microridge surface demonstrate slip velocity behavior consistent with that observed on the 60-60 surface, but reduced in magnitude. Reynolds numbers range from 4970 (\circ) to 7930 (∇). Larger feature spacing performs better for a given Reynolds number. Reynolds numbers are: 4970 (\circ), 5400 (\blacklozenge), 6800 (Δ), 7160 (\blacksquare), 7930 (∇). The modified Spalding fits (—) are overlaid on the profile corresponding to $Re=7930$.

Figure 6.

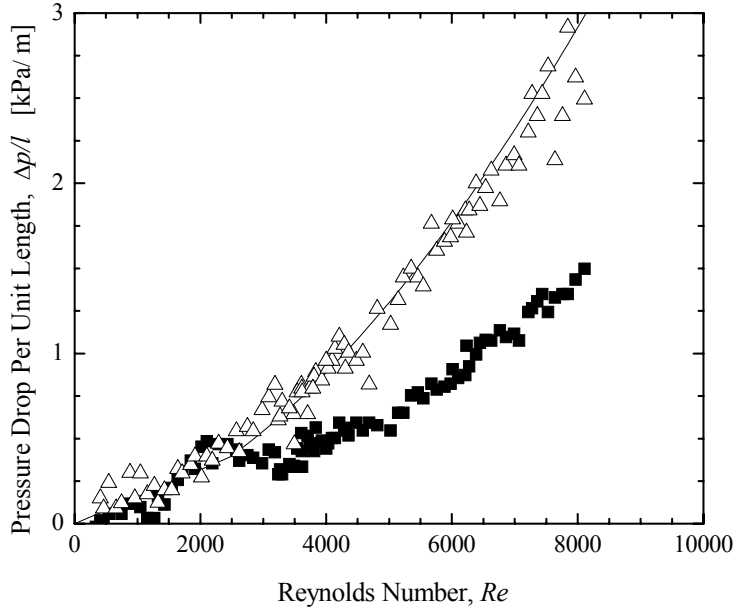


Figure 6. Pressure drop measurements for flow through a rectangular channel with a smooth walls (Δ) and with two walls containing superhydrophobic microridges with $w=60\mu\text{m}$ and $d=60\mu\text{m}$ (\blacksquare). The Colebrook line (—) is shown for a smooth channel.

Figure. 7.

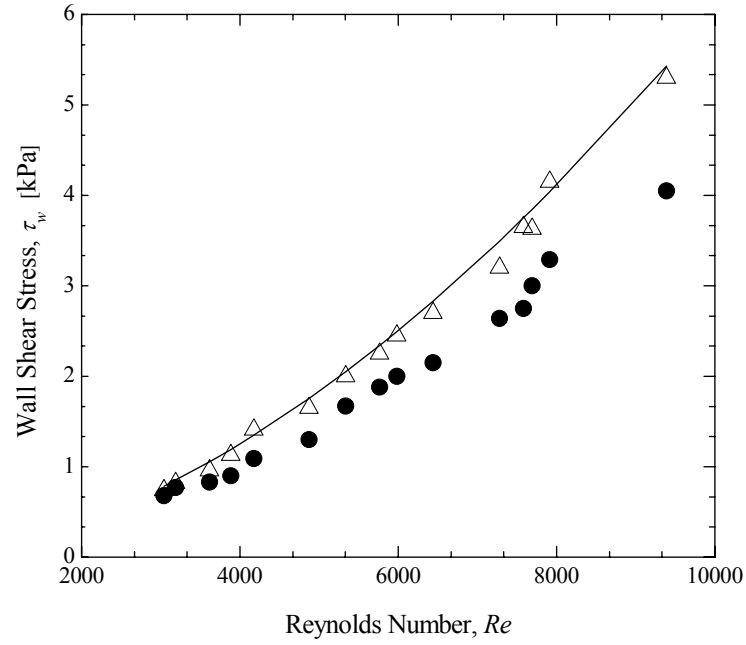


Figure 7. Wall shear stress measured from PIV as a function of Reynolds number for a channel with a single superhydrophobic surface. Results are presented for both the smooth top wall (Δ) and the superhydrophobic bottom wall containing $w=30\mu\text{m}$ wide ridges spaced $d=30\mu\text{m}$ apart (\bullet). Drag reduction is seen only on the superhydrophobic wall, the smooth wall being in good agreement with the Colebrook prediction for a smooth channel (—).

Figure 8.

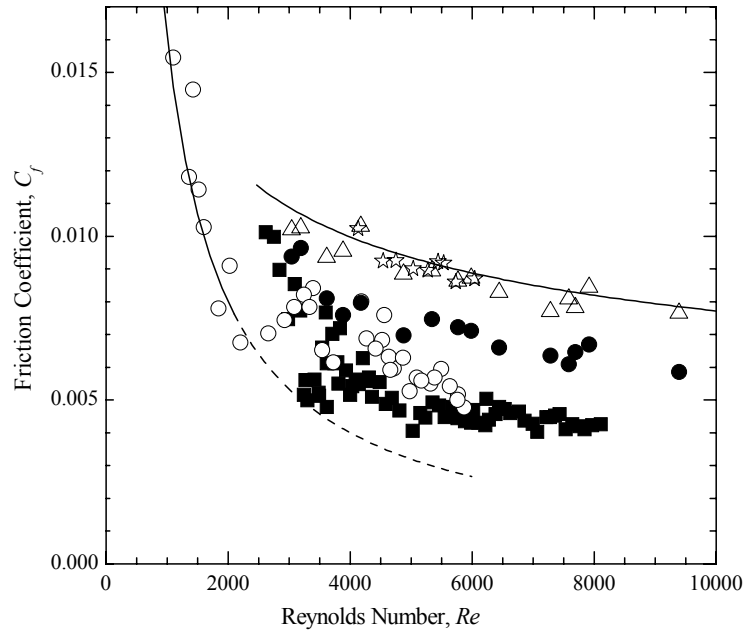


Figure 8. Coefficient of friction for various surfaces calculated from both PIV and pressure measurements. Smooth surfaces (Δ) and superhydrophobic surfaces containing $w=30\mu\text{m}$ wide microridge spaced $d=30\mu\text{m}$ apart (\bullet) are shown for PIV measurements of a channel with a single superhydrophobic wall. Pressure drop measurements from channels with two smooth walls (\star) and two superhydrophobic walls containing $w=30\mu\text{m}$ and $d=30\mu\text{m}$ microridges (\circ) and $w=60\mu\text{m}$ $d=60\mu\text{m}$ microridges (\blacksquare) are also shown. The predictions of the friction coefficient for a smooth channel is also shown (—) in both the laminar and turbulent regimes. Transition occurs around $Re = 2100$.

Figure 9.

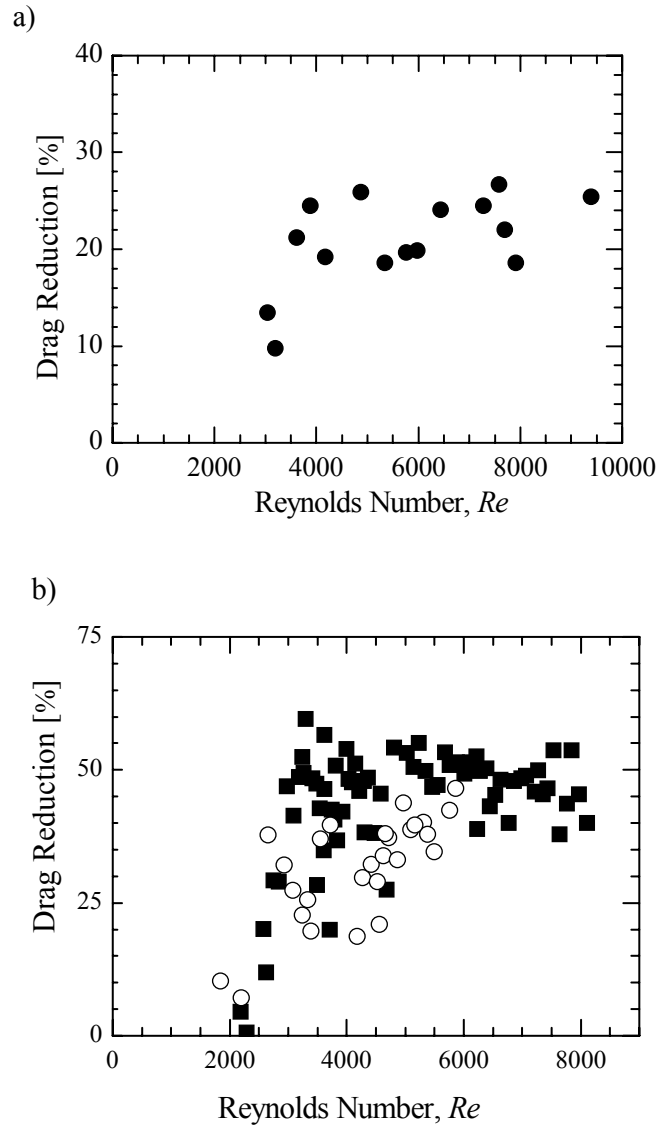


Figure 9. Drag reduction as a function of Reynolds number for a channel with a) a single superhydrophobic wall $w=30\mu\text{m}$ $d=30\mu\text{m}$ (●) and b) two superhydrophobic walls containing $w=30\mu\text{m}$ and $d=30\mu\text{m}$ microridges (○) and $w=60\mu\text{m}$ and $d=60\mu\text{m}$ microridges (■).

Figure 10.

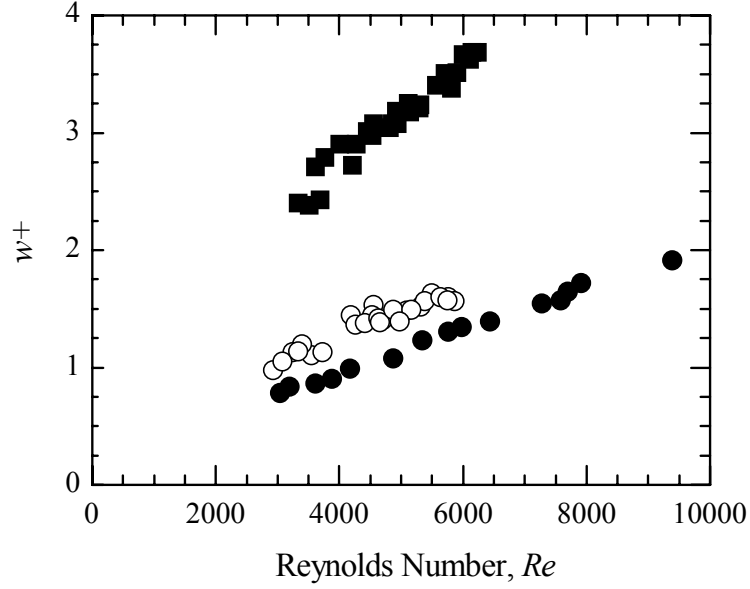


Figure 10. The microridge spacing in wall units, w^+ , as a function of Reynolds number. The data are taken from PIV measurements from a channel with a single superhydrophobic surface of $w=30\mu\text{m}$ and $d=30\mu\text{m}$ microridges (\bullet) and from pressure measurements for flow through a channel with two superhydrophobic walls containing $w=30\mu\text{m}$ and $d=30\mu\text{m}$ microridges (\circ) and $w=60\mu\text{m}$ and $d=60\mu\text{m}$ microridges (\blacksquare). A spacing of $w^+ = 5$ corresponds to the thickness of the viscous sublayer. Only points in the turbulent regime are shown.